NUCL SCI TECH (2020) 31:63
https://doi.org/10.1007/s41365-020-00775-w

Effect of the draw ratio in dry jet-wet spinning on aromatic copolysulfonamide fibers

Jian-Ning Wang[1] · Yu-Mei Zhang[1] · Xiao-Yun Li[2]

Received: 29 January 2020 / Revised: 7 April 2020 / Accepted: 27 April 2020 / Published online: 16 June 2020

Abstract Aromatic copolysulfonamide (*co*-PSA) fiber produced via wet spinning exhibits poor mechanical properties. Hence, dry jet-wet spinning was introduced to prepare the *co*-PSA fiber. Dry jet-wet spinning exhibits the advantage of positive stretching to the extruded fiber before coagulation. The fibers were spun at different jet draw ratios and second draw ratios and were examined for scanning electron microscopy, mechanical properties, sound velocity, small-angle X-ray scattering (SAXS), and wide-angle X-ray scattering (WAXS). The results revealed that all the fibers exhibited a uniform and dense structure and nearly round cross section at different drawing conditions. The strength and orientation of the fiber increased slightly as the jet draw ratio was increased to the second draw ratio of 2.0. Furthermore, the fibers formed a periodic ordered structure along the fiber axis. However, the strength of the fibers decreased significantly when the jet draw ratio continued to increase and the second draw ratio decreased year-on-year to maintain the total draw ratio at 11.0. Additionally, the fibers exhibited lower orientation because the molecular chain segments could not continue to extend and orient even at larger jet draw ratios, and thus they could not be further well-stretched at subsequent lower stretching ratios. Meanwhile, the periodic ordered structure disappeared and more content of entanglement structure existed in the fibers. During the heat drawing process, the results of SAXS and WAXS indicated that the better ordered molecular chain segments within the fiber were easier to arrange and reconstruct to significantly improve the content of crystalline and mesophase structures in the fibers. Hence, after the heat drawing process, the strengths of *co*-PSA-H2 and *co*-PSA-H3 fibers increased to more than 620 MPa, which is significantly higher than those of commercialized fibers and fibers reported in extant studies.

Keywords Aromatic copolysulfonamide fibers · Dry jet-wet spinning · Draw ratio · Morphology and performance

1 Introduction

Aromatic polysulfonamide (PSA) fiber is a high-performance polymer fiber, with excellent high temperature resistance and flame retardancy [1, 2]. It exhibits several typical structures, such as poly(4, 4′-diphenylsulfonyl terephthalamide) (*pt*-PSA), poly(3, 3′-diphenylsulfonyl terephthalamide) (*mi*-PSA), and aromatic copolysulfonamide (*co*-PSA) [3, 4]. The PSA fibers can be spun via dry spinning [5], wet spinning [6, 7], and dry jet-wet spinning [8] methods.

This study was financially supported by the National Natural Science Foundation of China (Nos. 11079015, 51273039 and 11705269), the Fundamental Research for the Central Universities (No. CUSF-DH-D-2016044), and Shanghai Sailing Program (No. 17YF1423800).

Electronic supplementary material The online version of this article (https://doi.org/10.1007/s41365-020-00775-w) contains supplementary material, which is available to authorized users.

✉ Jian-Ning Wang
1152052@mail.dhu.edu.cn

[1] State Key Laboratory for Modification of Fibers and Polymer Materials, College of Material Science and Engineering, Donghua University, Shanghai 201620, China

[2] Shanghai Synchrotron Radiation Facility, Shanghai Advance Research Institute, Chinese Academy of Sciences, Shanghai 201210, China

Banduryan et al. [5] and Sokira et al. [7] reported that the tensile strength of *pt*-PSA fibers is 4.0 cN/dtex and 3.27 cN/dtex when prepared via dry spinning and wet spinning methods, respectively. Wet-spun *pt*-PSA fibers exhibit a porous structure, which is distinguishable from the dry-spun fibers with the nonporous high-tenacity structures. However, the stability to cyclic shear stresses of the wet-spun fibers is twice that of the dry-spun fibers due to the micro-heterogeneous structure. The tenacity of wet-spun *pt*-PSA fibers can be increased up to 4.4 cN/dtex [9] by increasing the thermal-drawn ratio. Furthermore, extant studies also revealed that the tenacity of wet-spun *mi*-PSA fibers can also be increased up to 4.4 cN/dtex [10]. However, due to a variety of industrialization considerations, both the *pt*-PSA and *mi*-PSA fibers have not been commercialized. Currently, for commercial fibers, cost and performance factors are taken into account to form a copolymer structure (*co*-PSA). Hence, they exhibit a strength of 2.8–3.5 cN/dtex [2, 11]. Based on the thermal-drawn conditions in a laboratory, the tenacity and elongation of the *co*-PSA fibers are as high as 4.6 cN/dtex and 16% [12, 13], respectively. Hence, it is evident that the cost to improve the failure strength involves sacrificing the failure elongation, which implies reducing the flexibility of the fiber. However, this is not good for the textile fiber. Therefore, in previous studies, the *co*-PSA fibers were prepared via dry jet-wet spinning to optimize the mechanical properties [8]. The length of air gap was set as 40 mm, and the first draw ratio was fixed as 2.17. The structure and property tests of the fiber along the spinning line revealed that both the orientation degree and strength of nascent fiber are much higher than that produced via wet spinning, and the heat-drawn fiber strength exceeded 520 MPa. However, many process parameters still require optimization to improve the properties of *co*-PSA fibers produced via dry jet-wet spinning.

As shown in previous studies [14–16], the properties of fibers are influenced by many processing parameters in dry jet-wet spinning. They mainly include the spinning temperature, air gap, coagulation condition, and draw ratio. Among these parameters, the increase in the draw ratio can significantly improve the orientation and crystallization degree of fibers, especially for high-viscosity spinning solution system, including cellulose [17], polyacrylonitrile (PAN) [15], poly(*p*-phenylene terephthalamide) PPTA [18], and poly(*p*-phenylene benzobisoxazole) PBO [19] fibers. Therefore, the draw ratio is the key to improving the mechanical properties of fibers during the dry jet-wet spinning process. Cellulose fibers [14] exhibit higher strength, modulus, and crystallinity when the first draw ratio increases from 4.2 to 8.4, and the cross section of the fibers is dense and circular. The structure of nascent PAN fibers showed that the cross section of fibers exhibits kidney-like shape at the low first draw ratio and a nearly circular shape at the higher first ratio. Hence, this demonstrated the importance of draw ratio [15]. Additionally, the total draw ratio increases with an increase in the first draw ratio to a certain range. However, the total draw ratio decreases when the first draw ratio increases further, thereby indicating that there is an optimal range for the first draw ratio [20].

Based on the aforementioned extant studies, the draw ratio has a significant impact on the morphology and properties of the fiber during dry jet-wet spinning process. It can be predicted that the jet draw ratio and second draw ratio are also important process parameters. However, the mechanism for this is not clear for dry jet-wet spinning of *co*-PSA solution. To understand this, the effects of the jet draw ratio and second draw ratio on the structure and performance of dry jet-wet spinning *co*-PSA fiber before and after heat stretching were investigated via scanning electron microscopy (SEM), sound velocity, small-angle X-ray scattering (SAXS), and wide-angle X-ray scattering (WAXS).

2 Experiments

2.1 Materials

The *co*-PSA solution was supplied by Shanghai Tanlon Fiber Co. Ltd. It was synthesized via polycondensation of 4,4′-diaminodiphenylsulfone (4,4′-DDS), 3,3′-diaminodiphenylsulfone (3,3′-DDS) and terephthaloyl chloride (TPC), with a monomer mole ratio of 3:1:4 in N'N-dimethylacetamide (DMAc) at low temperature. The intrinsic viscosity (η) of the synthesized *co*-PSA was 1.8 dL g^{-1}, which was measured in a dimethyl sulfoxide (DMSO) at 25 °C. The concentration of *co*-PSA in the spinning dope was 23 wt%, and the viscosity of the spinning dope was 349 Pa s at 40 °C.

2.2 Dry jet-wet spinning

The *co*-PSA fibers were spun via a dry jet-wet spinning technique on a laboratory spinning line. The spinning dope temperature was maintained at 40 °C. The *co*-PSA solution was filtered and pumped through a 40-hole spinneret of 0.15-mm diameter at a flow rate of 3.2 m/min. Subsequently, it was passed through an air gap of 30 mm through which it finally entered a coagulation bath (DMAc/H_2O, v/v) with a concentration and temperature of 40% and 50 °C, respectively. Subsequently, the nascent gel filaments were further drawn into the second bath with deionized water at 60 °C and the third bath with boiling deionized water. The third draw ratio (λ_3) was maintained

as 1.05 without change. The jet stretch (λ_1) was increased from 3.5 to 5.5, the second draw ratio (λ_2) was maintained as 2.0, and the sample was labeled as *co*-PSA-1 ~ *co*-PSA-3. Subsequently, λ_1 continued to increase from 5.5 to 8.5 and λ_2 decreased year-on-year to maintain the total draw ratio as 11.0. The sample number was labeled as *co*-PSA-3 ~ *co*-PSA-6, as shown in Table 1. The samples of *co*-PSA-1 ~ *co*-PSA-4 were first dried at 150 °C with a draw ratio of 1.05. Furthermore, heat stretching was conducted at 365 °C with a draw ratio of 2.0, and finally thermal setting was conducted at 260 °C with a draw ratio of 1.04. The corresponding sample label was *co*-PSA-H1 ~ *co*-PSA-H4.

2.3 Characterization

The cross-sectional characteristics of the *co*-PSA fibers were examined via SEM (S-3000 N, Hitachi, Japan). The cross sections of the filament axis of approximately 2-mm thickness were prepared using a Hardy fiber microtome. The samples for cross-sectional features were prepared in liquid nitrogen and sputtered with gold prior to analysis.

The mechanical properties of the *co*-PSA fibers were directly recorded without any treatment using a tensile tester (XQ-1A, Shanghai New Fiber Instrument Co., Ltd, China) with a gage length of 10 mm and an extension rate of 10 mm/min. A minimum of 30 filaments were tested in each case for the tensile tests.

The sound velocity (C) was determined via the sound velocity orientation tester of SCY-III with a tension of 0.1 gf/dtex. The *co*-PSA fibers were placed on the sample rack with a length of 60 cm. Subsequently, the *co*-PSA fibers were mounted between two transducers composed of a piezoelectric ceramic crystal with a natural frequency of 5 kHz. The velocity of the longitudinal wave in the material was measured by placing the fiber between the two transducers. The sound velocity was measured by measuring the length and time from the recorder. The measurement was repeated five times.

Furthermore, SAXS experiments were conducted on a beam line (BL16B) at Shanghai Synchrotron Radiation Facility (SSRF) with an X-ray wavelength of 0.124 nm. The sample-to-detector (Mar CCD 165) distance was set as 1980 mm. All the data analyses were performed using the xPolar software (Precision works NY, Inc., USA). The average scattering object length (l), misorientation angle (B_Φ), and long axis-to-short axis ratio (LA/SA) were calculated as reported in extant studies [8, 21].

Additionally, WAXS was performed at SSRF with the same equipment as SAXS. A bundle of *co*-PSA fibers was placed on a sample holder with the fiber direction perpendicular to the X-ray beam. Two-dimensional (2D) WAXS patterns were acquired using a Mar CCD (165) detector. The specimen-to-detector distance was set to 171.7 mm. All the data analyses were conducted using the xPolar software (Precision works NY, Inc., USA). Quantitative evaluation of the phase fraction was determined from the corrected WAXS pattern, as described by Che et al. [22] and Ran et al. [23]. The amorphous and crystal orientation along the fiber axis was calculated based on the methods described in an extant study [21].

3 Results and discussion

3.1 Effect of jet stretch on the property and morphology of *co*-PSA fibers

The concentrated solution was directly used as the spinning dope. During dry jet-wet spinning experiments, it was observed that the maximum jet stretch can reach up to 8.5, while the maximum second draw ratio was 1.3, and the total draw ratio was approximately 11.0, which is much higher than that of wet spinning [21]. Theoretically, increasing the draw ratio is an effective way to improve the mechanical properties of the fiber. However, this is limited by the molecular weight, concentration of the polymer, and the rheological properties of the *co*-PSA solution. Furthermore, the draw ratio of dry jet-wet spinning can only be controlled within a certain range. Therefore, different jet draw ratios and second draw ratios were designed, and the effect of different draw ratios on the structure and performance of *co*-PSA fibers was studied before and after heat stretching.

Table 1 *co*-PSA fibers prepared under different draw ratio conditions

Sample	Jet stretch ratio/λ_1	Second draw ratio/λ_2	Total draw ratio/λ_t
co-PSA-1	3.5	2.0	6.0
co-PSA-2	4.5	2.0	8.0
co-PSA-3	5.5	2.0	11.0
co-PSA-4	6.5	1.7	11.0
co-PSA-5	7.5	1.5	11.0
co-PSA-6	8.5	1.3	11.0

3.1.1 *Effect of jet stretch on the property and morphology of co-PSA fibers before heat stretching*

The jet draw ratio (λ_1) was increased from 3.5 to 5.5, and the second draw ratio (λ_2) and third draw ratio (λ_3) remained constant at 2.0 and 1.05, respectively. It was observed that the spinning was conducted smoothly when the jet stretch ratio increased to 5.5. However, breaking of filaments and unstable spinning occurred when the spinning velocity continued to increase year-on-year.

The tenacity, initial modulus, and elongation at break for *co*-PSA fibers under different jet stretch ratios are listed in Table 2. The results show that with the increase in the jet draw ratio from 3.5 to 5.5, the strength and modulus of *co*-PSA fibers increase from 116 MPa and 1.65 GPa to 126 MPa and 2.33 GPa and then decrease to 119 MPa and 2.2 GPa, respectively, and the elongation decreases. Due to the steric hindrance effect and non-planar structure of the sulfone groups within the PSA molecular chains, a "straight line" structure cannot be formed in both the solution and solid states. Furthermore, it is difficult for PSA filament to obtain a high orientation structure via stretching once it is coagulated due to the presence of amide bond in PSA molecules. Therefore, the strength of *co*-PSA fibers does not significantly change, and the modulus of the fibers increases slightly when the jet draw ratio is higher than 3.5.

The cross section and surface of *co*-PSA fibers in different jet draw ratios are shown in Fig. 1. The cross sections of the *co*-PSA fibers are nearly circular. The structure of fibers is dense and uniform, and the surface is almost smooth. However, there are very shallow grooves in the local area along the fiber. This may be due to the friction between the high-speed moving fiber and godet roller in the high velocity spinning process. Figure 1 also shows that the diameter of *co*-PSA-1 ~ *co*-PSA-3 fibers decreases significantly with increases in the jet draw ratio. Given that there are no obvious defects inside or on surface of the fibers, the difference in the mechanical properties of the fibers should be attributed to the microstructure and orientation of the PSA molecular chain aggregates. Based on previous studies [8], such cross section and structure are more conducive to subsequent stretching and improvement in fiber performance via heat stretching.

Table 2 Mechanical properties of *co*-PSA fibers at different jet stretch ratios

Sample	Tenacity (MPa)	Modulus (GPa)	Elongation (%)
co-PSA-1	116 ± 9	1.65 ± 0.13	28.2 ± 1.9
co-PSA-2	126 ± 10	2.33 ± 0.28	27.6 ± 1.3
co-PSA-3	119 ± 9	2.20 ± 0.25	23.9 ± 1.8

The orientation of PSA fibers cannot be tested via birefringence because it exhibits strong absorption of visible light. Thus, the oriented structure of the *co*-PSA fibers was quantified via SAXS and WAXS, as shown in Figs. 2 and 3, respectively. The SAXS patterns exhibited a sharp and elongated equatorial streak that was superimposed with a relatively weak and short meridional intensity distribution. The results indicated that the internal microstructure of the fiber is aligned parallel to the direction of the filaments, and a periodic ordered structure is formed in the fiber along the fiber axis [24–26]. Figure 3 shows that the halo tended to centralize along the equator, which illustrates that only an amorphous structure exists and acquires a degree of orientation within the *co*-PSA fibers.

The structural parameters of *co*-PSA fibers calculated via a 2-D image analysis method, as described by Yu et al. [21], as well as the sound velocity, are listed in Table 3, where the misorientation angle B_ϕ and long axis-to-short axis ratio (LA/SA) were calculated via SAXS patterns (Fig. S1). Furthermore, the amorphous orientation f_a was calculated via WAXS patterns (Fig. S2), and the sound velocity C was tested as described above. Higher values of LA/SA, f_a, and C indicate a larger orientation of *co*-PSA, and the tendency of B_ϕ is contrary. Furthermore, B_ϕ, LA/SA, and C demonstrate the orientation of scattering objects of microfibril and voids, while f_a shows the orientation of molecular chain segments in the amorphous phase. Hence, B_ϕ decreased from 30.4 to 28.5, and LA/SA, C, and f_a increased when jet draw ratio increased from 3.5 to 4.5. This implies an increase in the orientation of *co*-PSA fiber. However, if the jet draw ratio is improved to 5.5, then LA/SA, C, and f_a slightly decrease but are still higher than those due to a jet draw ratio of 3.5. The tendency of orientation is consistent with the mechanical properties. Thus, the results also indicated that some chains exhibit only 1D or 2D ordering and pack along the fiber axis to form the mesophase structure [21]. However, given the unique molecular structure of PSA, as mentioned above, the amorphous orientation f_a is changed slightly, thereby illustrating that the PSA chain segments are still difficult to orient as the jet draw ratio is increased to 5.5. Additionally, for *co*-PSA-1 ~ *co*-PSA-3 fibers, the fitting curve provides a negative intercept, and this illustrates that the scattering objects are large enough over a certain length. This is due to the uniaxial tension during the spinning process.

3.1.2 *Effect of jet stretch on property and morphology of co-PSA fibers after heat stretching*

Based on the results obtained by Yu et al. [12, 13, 21], the molecular chains cannot be reconstructed and

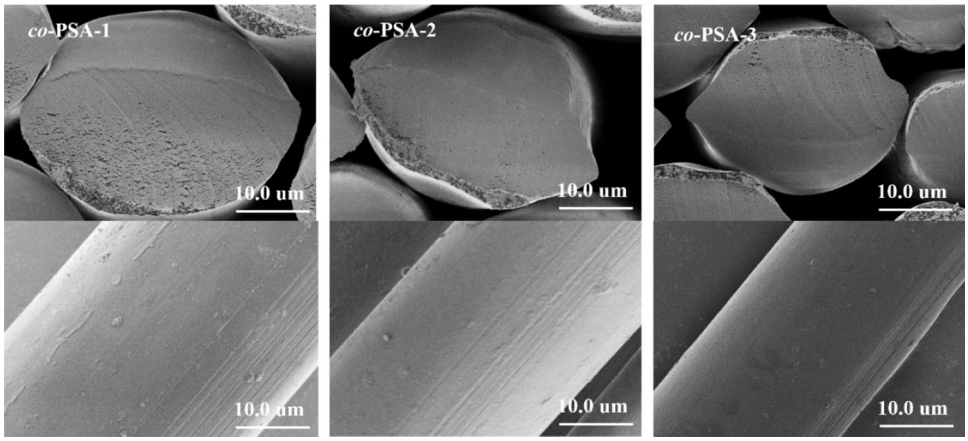

Fig. 1 SEM images of *co*-PSA fibers at different jet draw ratios (λ_1 increase from 5.5 to 8.5, λ_2 = 2)

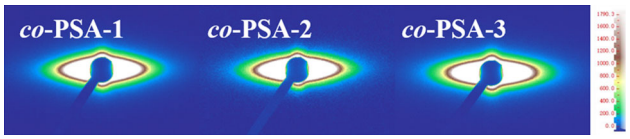

Fig. 2 (Color online) SAXS patterns of *co*-PSA fibers at different jet draw ratios (λ_1 increases from 5.5 to 8.5, λ_2 = 2)

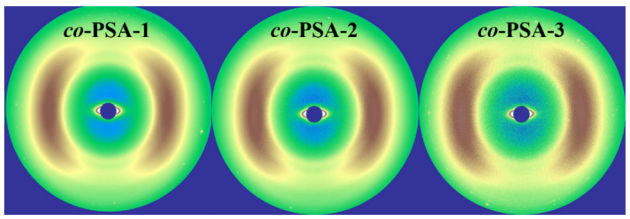

Fig. 3 (Color online) WAXS patterns of *co*-PSA fibers at different jet draw ratios (λ_1 increases from 5.5 to 8.5, λ_2 = 2)

Table 3 Parameters from SAXS and WAXS patterns and sound velocities

Sample	B_{ϕ}^{a} (°)	LA/SA^{b}	f_{a}^{c}	C (km/s)
co-PSA-1	30.4	2.58	0.31	2.15
co-PSA-2	28.5	2.79	0.33	2.20
co-PSA-3	29.8	2.63	0.32	2.16

[a]Misorientation angle of the scattering object was calculated via SAXS patterns

[b]Long axis (equator) to short axis (meridian) ratio (LA/SA) of scattering ring in SAXS patterns

[c]Amorphous orientation along the fiber axis was calculated via WAXS patterns

crystallized in time when the thermal stretching ratio is higher than 2.0 times because of insufficient residence time for the fiber to stay in the heat tube. Furthermore, the fiber exhibits the highest strength when the temperature of the heat stretching process is approximately 370 °C. Therefore, the heat-drawn temperature and stretching ratio were set to 365 °C and 2.0 times, respectively. After heat drawing, the structure and properties of the fiber samples *co*-PSA-H1 to *co*-PSA-H3 were tested.

The mechanical properties of *co*-PSA fibers with respect to different jet draw ratios are listed in Table 4. The results indicated that the strength and modulus of *co*-PSA fibers improved significantly after the same heat stretching process. Furthermore, previous studies demonstrated that the crystalline structure can only be formed in PSA fibers after heat drawing above the glass transition temperature. Thus, the strength of the heat-drawn fiber is significantly improved. Although the strengths of *co*-PSA-1 ~ *co*-PSA-3 fibers changed slightly, the heat-drawn fibers of *co*-PSA-H2 ~ *co*-PSA-H3 exhibit a tenacity of 627 MPa and 623 MPa, respectively, which are higher than that of the *co*-PSA-H1 fiber. The strengths of *co*-PSA-H3 fiber and *co*-PSA-H2 fiber are approximately the same and are much higher than that of commercial fibers [21] and those of fibers reported in extant studies [12, 13]. Hence, the results fully demonstrated that the performance *co*-PSA fibers can be further improved by increasing the jet draw ratio of dry jet-wet spinning. Thus, a higher jet draw ratio leads to a higher orientation of fiber before and after the heat drawn is higher. Moreover, the mechanical properties of *co*-PSA fiber are also related to the crystal structure. Therefore, the structural parameters of the fibers were characterized via SAXS and WAXS.

Table 4 Mechanical properties of heat-drawn *co*-PSA fibers at different jet draw ratios

Sample	Tenacity (MPa)	Modulus (GPa)	Elongation (%)
co-PSA-H1	558 ± 44	6.58 ± 0.48	17.0 ± 1.8
co-PSA-H2	627 ± 24	7.12 ± 0.23	15.2 ± 1.0
co-PSA-H3	623 ± 33	7.03 ± 0.50	14.6 ± 1.0

Figure 4 shows that the equatorial streak of the heat-drawn *co*-PSA fibers becomes sharper and the intensity is increased, thereby indicating a higher orientation of the fibers. Moreover, the SAXS patterns show a weak meridional arc-shape scattering, which demonstrates the existence of a periodic structure in the draw direction [27]. Based on the SAXS patterns of heat-drawn *co*-PSA fibers, the average fibril length (l), fibril misorientation (B_ϕ), and the long axis-to-short axis ratio (LA/SA) are determined (Fig. S3) and listed in Table 5. When compared to fibers before heat drawing, the value of B_ϕ of heat-drawn fibers decreases from approximately 30–10, and the value of LA/SA increases from approximately 2.6–3.3. This indicates a significant improvement in orientation because the internal structure of the low orientation begins to reconstruct to form the high orientation fibril structure. However, the fibril length of *co*-PSA-H1 is 353, which is shorter than that of *co*-PSA-H2 and *co*-PSA-H3. This is mainly because of the high orientation and extended PSA chain segments that can be easily inclined to pack into a crystal lattice to form a longer fibril structure in the heat-drawn process [23].

The amorphous and crystalline structure in the nanometer scale was analyzed via WAXS, as shown in Fig. 5. The WAXS patterns of heat-drawn *co*-PSA fibers exhibited an obvious development of the equatorial, meridional, and off-axis (*hkl*) reflections following the heat stretching. The reflections became sharper with an increase in the jet draw ratio even in the same heat-drawn conditions, thereby indicating the development of a crystalline structure within the fibers [13, 28]. To illustrate the development of the crystalline structure, a two-dimensional image analysis method, as described by Yu et al. [13, 21], is used to extract quantitative information of crystal, amorphous, and mesomorphic fractions from 2D WAXS patterns (Fig. S4), as listed in Table 6. The content of the amorphous phase is less than 20%, and the content of mesophase and content of crystal phase are more than 45% and 30%, respectively, in heat-drawn fibers. The crystal orientation is more than 0.95. Given that the fibers of *co*-PSA-2 and *co*-PSA-3 exhibit a higher oriented structure at higher jet draw ratios, a better oriented molecular chain segment is more likely to move into the lattice and form a higher crystal structure during the heat drawing process. This leads to the formation of a more perfect structure with higher fractions of mesophase and crystal phase with a higher degree of crystal orientation. Thus, the fibers of *co*-PSA-H2 and *co*-PSA-H3 exhibit better mechanical properties than *co*-PSA-H1.

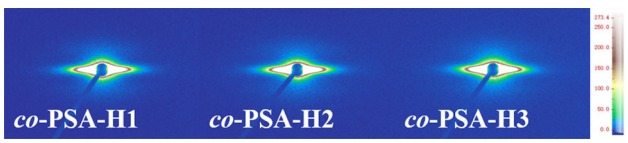

Fig. 4 (Color online) SAXS patterns of heat-drawn *co*-PSA fibers at different jet draw ratios (λ_1 increases from 5.5 to 8.5, $\lambda_2 = 2$)

Table 5 Results from SAXS patterns

Sample	l^a (nm)	B_ϕ (°)	LA/SA
co-PSA-H1	353	11.46	3.2
co-PSA-H2	362	9.9	3.4
co-PSA-H3	372	10.0	3.3

[a]Average fibril length l of *co*-PSA fibers

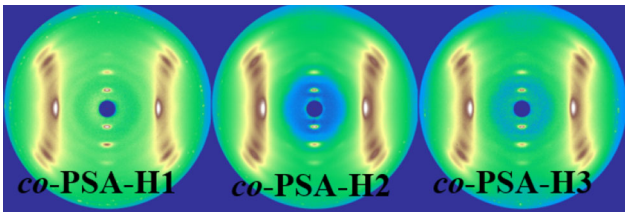

Fig. 5 (Color online) WAXS patterns of heat-drawn *co*-PSA fibers at different jet draw ratios (λ_1 increases from 5.5 to 8.5, $\lambda_2 = 2$)

Table 6 Structural parameters from WAXS patterns

Sample	*co*-PSA-H1	*co*-PSA-H2	*co*-PSA-H3
Amorphous fraction (%)	20	14	16
Mesophase fraction (%)	47	50	49
Crystal fraction (%)	33	36	35
Crystal orientation f_c	0.96	0.98	0.97

3.2 Effect of jet stretch and second stretch on property and morphology of *co*-PSA fibers

3.2.1 Effect of jet stretch and second stretch ratio on property and morphology of co-PSA fibers before heat stretching

The filaments are prone to fracture when the jet draw ratio is more than 5.5 at the second draw ratio of 2.0. On the premise of smooth spinning and to further increase the jet draw ratio, the second draw ratio decreased year-on-year to maintain the total draw ratio of 11.0. The mechanical properties of *co*-PSA fibers at different jet draw ratios and second draw ratios are shown in the Table 7.

As per previous studies [14, 29], the high jet draw ratio is conducive to the improvement in the orientation and mechanical properties of fibers. On the premise of smooth spinning, the jet draw ratio continued to increase from 5.5 to 8.5, the second draw ratio decreased year-on-year from

Table 7 Mechanical properties of *co*-PSA fibers at different stretching ratios

Sample	Tenacity (MPa)	Modulus (GPa)	Elongation (%)
co-PSA-3	119 ± 9	2.20 ± 0.25	23.9 ± 1.8
co-PSA-4	92 ± 10	1.90 ± 0.12	32.3 ± 2.5
co-PSA-5	77 ± 5	1.17 ± 0.07	35.8 ± 1.5
co-PSA-6	72 ± 6	1.10 ± 0.14	38.7 ± 2.7

2.0 to 1.3, and the total draw ratio was maintained at 11.0. However, it was observed that the strengths of *co*-PSA-3 to *co*-PSA-6 continued to decrease from 119 MPa to 72 MPa. The strengths of *co*-PSA-5 and *co*-PSA-6 fibers were less than 80 MPa and decreased by approximately 30% when compared to *co*-PSA-3. Hence, when λ_1 was higher than 8.5, the filament was broken and spinnability was poor. This indicated that in the PSA/DMAc spinning system, the improvement in the strength of *co*-PSA fibers is limited and can only be enhanced via increasing the jet draw ratio while a high second draw ratio is also required. To further explain the reasons, the structural changes in the *co*-PSA fibers were investigated.

The cross section and surface of *co*-PSA fibers under different stretching ratios are shown in Fig. 6. The fibers are dense and uniform, and the part of surface has shallow grooves along the fiber axis. There was no significant change in the diameter of the fibers when λ_1 was increased and λ_2 was decreased year-on-year to maintain a constant value of λ_t. There were no obvious defects in the fiber, thereby indicating that the difference in the mechanical properties between the fibers was mainly related to the different orientation degrees of the fibers.

The orientation of *co*-PSA fibers was measured via SAXS, WAXS, and sound velocity. Specifically, the SAXS and WAXS patterns of *co*-PSA fibers under different stretching ratios are shown in Figs. 7 and 8, respectively, and B_ϕ, LA/SA, f_a, and C are calculated as Fig. S5 and Fig. S5 and then listed in Table 8. The SAXS and WAXS patterns of the *co*-PSA fibers exhibit oriented structure when λ_1 increases and λ_2 decreases year-on-year. However, when compared to *co*-PSA-3 fiber, the SAXS patterns exhibit a shorter equatorial streak and the vanishing meridional scatters for *co*-PSA-4 to *co*-PSA-6 fibers, thereby indicating that the degree of orientation decreases and no periodic structure exists in these fibers.

Table 8 shows the quantitative analysis of orientation of *co*-PSA fibers. The results show that B_ϕ increases from 29.8 to 34.9, and the *LA*/*SA* and sound velocity decrease from 2.63 to 2.35 and from 2.16 to 1.84, respectively. This clearly indicates the decrease in orientation of the scattering objects. Meanwhile, f_a decreases from 0.32 to 0.29, thereby suggesting a low orientation of the amorphous region within the fiber. Hence, the results demonstrate that it is difficult for PSA molecular segments to further increase the orientation and withstand higher stretching even when λ_1 is increased from 5.5 to 8.5. Furthermore, given that λ_2 decreases year-on-year, the orientation of the fiber in the second stretching process was low. Thus, the overall orientation of the fiber was low and the strength of *co*-PSA fiber decreased. Hence, the results indicated that a higher second draw ratio is an important condition for the formation of a PSA fiber structure with better orientation and the formation of a periodic structure within the fibers.

3.2.2 *Effect of jet stretch and second stretch on property and morphology of co-PSA fibers after heat stretching*

The thermal stretching ratio was below 2.0 times. In the case of the *co*-PSA-5 and *co*-PSA-6 fibers, the strength is low and the elongation is large. However, the improvement in the strength was limited even if the subsequent heat stretching ratio was higher than 2.0 times. Therefore, only *co*-PSA-3 and *co*-PSA-4 fibers were chosen for the heat drawing process, and their structure and properties were characterized. The tenacity, initial modulus, and elongation at break of the heat-drawn *co*-PSA-H3 and *co*-PSA-H4 fibers under different jet and second stretching ratios are shown in Table 9. The strength of the *co*-PSA-H4 fiber corresponded to 484 MPa, which was nearly 30% lower

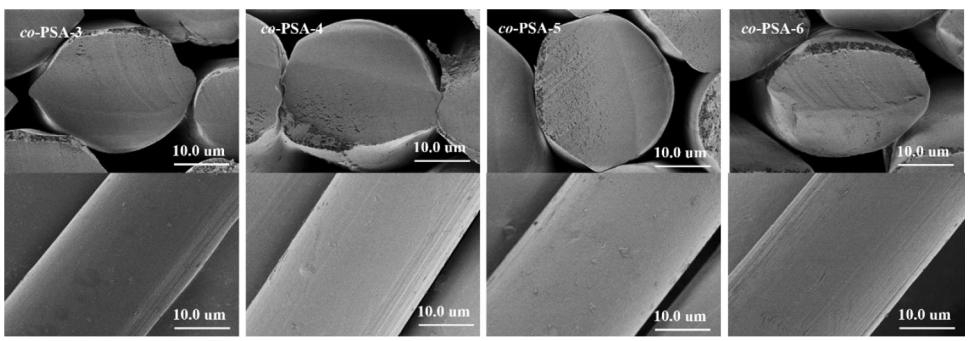

Fig. 6 SEM pictures of *co*-PSA fibers at different stretching ratios (λ_1 increases from 5.5 to 8.5, λ_2 decreases from 2.0 to 1.3 year-on-year; λ_t = 11.0)

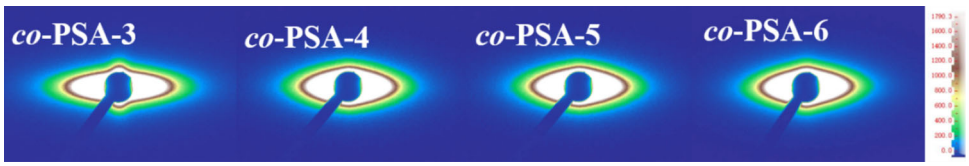

Fig. 7 (Color online) SAXS patterns of *co*-PSA fibers at different stretching ratios (λ_1 increases from 5.5 to 8.5, λ_2 decreases from 2.0 to 1.3 year-on-year; λ_t = 11.0)

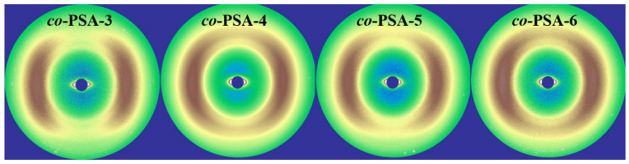

Fig. 8 (Color online) WAXS patterns of *co*-PSA fibers at different stretching ratios (λ_1 increases from 5.5 to 8.5, λ_2 decreases from 2.0 to 1.3 year-on-year; λ_t = 11.0)

Table 8 Parameters from SAXS and WAXS patterns and sound velocities

Sample	B_ϕ (°)	*LA*/*SA*	f_a	*C* (km/s)
co-PSA-3	29.8	2.63	0.32	2.16
co-PSA-4	33.9	2.44	0.30	2.04
co-PSA-5	34.5	2.42	0.29	1.87
co-PSA-6	34.9	2.35	0.29	1.84

Table 9 Mechanical properties of *co*-PSA fibers at different stretching ratios

Sample	Tenacity (MPa)	Modulus (GPa)	Elongation (%)
co-PSA-H3	623 ± 33	7.03 ± 0.50	14.6 ± 1.0
co-PSA-H4	484 ± 24	6.31 ± 0.45	22.4 ± 1.6

than that of *co*-PSA-H3 fiber. Thus, the results show that the fiber with lower strength before the heat drawing process still exhibits lower strength after the heat drawing process.

The SAXS and WAXS were used to characterize the microstructure parameters of the fibers after the heat drawing process to further explain the structural transformation of the fibers. As shown in Figs. 9 and 10, the SAXS patterns show that the scattering in the equatorial direction of *co*-PSA-H4 is less sharp than that of *co*-PSA-H3 fiber, and the "arc" scattering disappears in the meridian direction. This illustrates a lower orientation for *co*-PSA-H4, and thus the periodic ordered structure that forms inside all the fibers along the fiber axial direction after heat drawing. The WAXS patterns exhibited remarkable reflections of

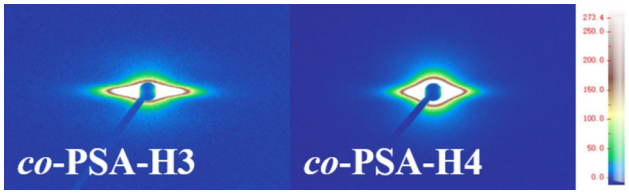

Fig. 9 (Color online) SAXS patterns of heat-drawn *co*-PSA fibers at different stretching ratios (*co*-PSA-H3: λ_1 = 5.5, λ_2 = 2.0; *co*-PSA-H4: λ_1 = 6.5, λ_2 = 1.7; λ_t = 11.0)

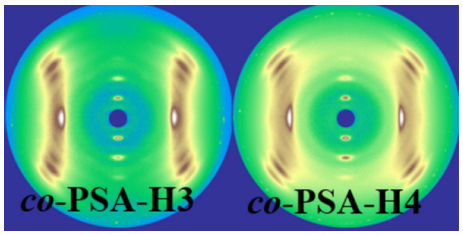

Fig. 10 (Color online) WAXS patterns of heat-drawn *co*-PSA fibers at different stretching ratios (*co*-PSA-H3: λ_1 = 5.5, λ_2 = 2.0; *co*-PSA-H4: λ_1 = 6.5, λ_2 = 1.7; λ_t = 11.0)

different axis, thereby indicating the formation of crystalline structure within the fibers following the heat stretching.

The quantitative analysis of orientation from SAXS patterns and fractions of crystal, amorphous, and mesomorphic phases from WAXS patterns (Figs. S3 and S4) are listed in Tables 10 and 11, respectively. In *co*-PSA-4 fiber, B_ϕ increases from 10 to 14.6 and LA/SA decreases from 3.3 to 2.1. This implies an obvious decrease in fibril orientation. Furthermore, the fibril length is also shorter because the mass fraction of the oriented structure is less in *co*-PSA-4 fiber when compared to that in *co*-PSA-H3 fiber. The content of the amorphous phase in *co*-PSA-H4 fiber significantly increases to approximately 30%, and the content of mesophase and crystal decreases to

Table 10 Results from the SAXS patterns

Sample	*l* (nm)	B_ϕ (°)	LA/SA
co-PSA-H3	372	10.0	3.3
co-PSA-H4	258	14.6	2.1

Table 11 Structural parameters from WAXS patterns

Samples	*co*-PSA-H3	*co*-PSA-H4
Amorphous fraction (%)	16	30
Mesophase fraction (%)	49	41
Crystal fraction (%)	35	29
Crystal orientation f_c	0.96	0.94

approximately 41% and 29%, respectively. This implies that it is more difficult to reconstruct, orient, and crystallize the molecular chain segments to form higher fractions of mesophase and crystal structure during the heat drawing process from the entangled structure within the *co*-PSA fiber before heat drawing.

To visualize the changes in the structure of *co*-PSA fibers before and after the heat drawing process under different jet and second stretching conditions, the microstructure of the fiber is characterized via SAXS and WAXS. Furthermore, the tangled and oriented structures of the molecular chain aggregation structure inside the fiber are shown in Figs. 11 and 12. The molecular chain orientation and entanglement structure are denoted by the red and blue colors in Fig. 11, respectively. When the jet draw ratio increases from 3.5 to 5.5, the *co*-PSA fibers exhibit high orientation. However, given the existence of the sulfone group and intermolecular amide bonds in PSA molecules, the molecular chain segments are hard to extend and orient to form higher mass fractions of the orientation structure. When the jet draw ratio continues to increase and the second draw ratio decreases year-on-year to maintain a total draw ratio, the molecular chain segments within the PSA-4 ~ *co*-PSA-6 fibers are still difficult to extend and orient to form a higher mass fraction of the orientation structure even at higher jet draw ratios. However, given that the second drawing is low, the entanglement structure cannot be stretched more, and thus has higher mass fraction. At the same time, as mentioned above, a periodic ordered structure is formed in PSA-1 ~ *co*-PSA-3 fibers. However, it disappears in PSA-4 ~ *co*-PSA-6 fibers because of the lower second stretching.

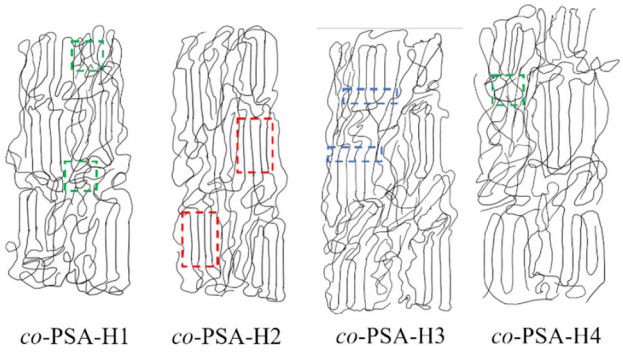

Fig. 12 (Color online) Molecular structure diagrams of heat-drawn *co*-PSA-H1 to *co*-PSA-H4 fibers under different stretching ratios (crystal, mesophase, and amorphous structure are denoted by red, blue, and green marks, respectively. *co*-PSA-H1 to *co*-PSA-H3: λ_1: 3.5 to 5.5, λ_2 = 2.0; *co*-PSA-H4: λ_1 = 6.5, λ_2 = 1.7, λ_t = 11.0)

As shown in Fig. 12, crystal, mesophase, and amorphous structure are denoted by red, blue, and green colors, respectively. The molecular chain segments, which are in a better orientation structure in fibers before heat drawing, are easier to orient to form higher mass fractions of crystalline and mesophase structures during the heat drawing process. Therefore, the mass fractions of crystalline and mesophase phases in PSA-H2 and *co*-PSA-H3 fibers are slightly than those in PSA-H1 fiber. Furthermore, the *co*-PSA-H4 fiber exhibits a higher content of amorphous structure because of the large content of entanglement structure within the *co*-PSA-4 fiber.

4 Conclusion

The effects of different jet draw ratios and second draw ratios on the morphology and properties of *co*-PSA fibers were investigated. The fibers had nearly round cross sections and were uniform and dense without obvious defect

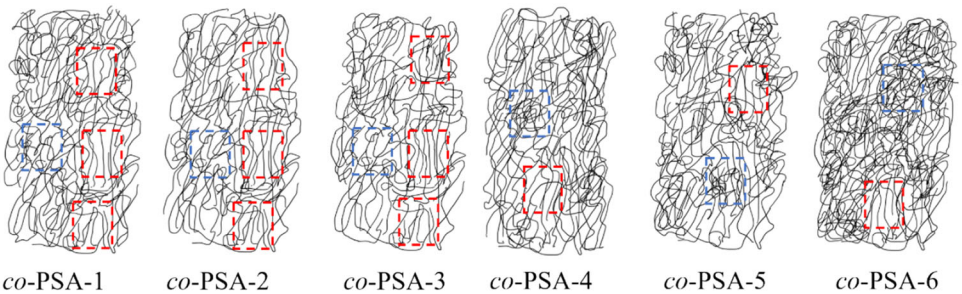

Fig. 11 (Color online) Molecular structure diagrams of *co*-PSA-1 to *co*-PSA-6 fibers under different stretching ratios (orientation and entanglement structure are denoted by red and blue marks, respectively. *co*-PSA-1 to *co*-PSA-3: λ_1: 3.5 to 5.5, λ_2 = 2.0; *co*-PSA-4 *co*-PSA-6: λ_1: 6.5 to 8.5, λ_2: 1.7 to 1.3, λ_t = 11.0)

structures. This was conductive to the subsequent stretching and heat stretching. As jet draw ratio increased, the strengths of the fiber changed slightly, and the orientations, as characterized via sound velocity, SAXS, and WAXS, also exhibited a slight change. However, the strengths and orientations of *co*-PSA-2 and *co*-PSA-3 fibers were slightly higher than those of *co*-PSA-1. A periodic ordered structure is formed in the fibers along the fiber axis. After heat drawing at 365 °C with a draw ratio of 2.0, it was observed that the high orientation of molecular chain segments in the fiber before heat drawing was easier to arrange and reconstruct under the heat drawing process. The content of amorphous phase was less than 20%, and the content of mesophase and content of crystalline phase were more than 45% and 30%, respectively, in the heat-drawn fibers. The degree of orientation of the crystal and non-crystal regions was also significantly improved. Hence, the strengths of *co*-PSA-H2 and *co*-PSA-H3 fibers increased to more than 620 MPa after the heat drawing process. The strengths of *co*-PSA-H2 and *co*-PSA-H3 fibers were significantly higher than those of commercialized fibers and fibers reported in previous studies.

The jet draw ratio continued to increase, and the second draw ratio decreased year-on-year, and thus the total draw ratio was maintained as constant. The strengths and orientations of *co*-PSA-4 ~ *co*-PSA-6 fibers decreased gradually because the molecular chain segments were difficult to extend and orient at higher jet draw ratios. Furthermore, the entanglement structure cannot be further stretched at subsequent lower stretching ratios. Additionally, the periodic ordered structure disappears, thereby indicating that more content of entanglement structure existed in the fibers. Therefore, even after high-temperature heat-drawing, it was difficult to arrange and reconstruct the molecular chain segments. Thus, the degree of crystallization and orientation was lower for *co*-PSA-H4 fiber. Furthermore, their mechanical properties were inferior.

References

1. X. Wang, Y. Zhang, Properties and application of aramid fibers. China Text. Lead. **1**, 18–23 (2005). https://doi.org/10.3969/j.issn.1003-3025.2005.01.003. (**in Chinese**)
2. B. Yan, Z. Yuhua, R. Jiarong, The application of polysulfonamide fiber in high temperature resistant filtration materials. Tech. Text. **12**, 33–36 (2006). https://doi.org/10.3969/j.issn.1004-7093.2006.12.010
3. G.A. Kuznetsov, N.I. Nikiforov, V.P. Lebedev et al., Investigation of the properties of some polysulphonamides in the condensed state. Polym. Sci. U.S.S.R. **16**, 3156–3162 (1974). https://doi.org/10.1016/0032-3950(74)90311-6
4. Y. Qian, C.B. Huang, Q.P. Ding et al., Terpolycondensation of 4, 4′-DDS/TPC/3, 3′-DDS and characterization. Polym. Mater. Sci. Eng. **22**, 42–45 (2006). https://doi.org/10.1016/S1872-2040(06)60046-7
5. S.I. Banduryan, N.A. Ivanova, S.G. Efimova et al., Dry- and wet-spun polysulfonamide fibres. Fibre Chem. **9**, 484–485 (1978). https://doi.org/10.1007/bf00546448
6. N.I. Muraveva, A.A. Konkin, Fibre from aromatic polysulphonamide. Fibre Chem. **3**, 612–615 (1971). https://doi.org/10.1007/bf00635769
7. A.N. Sokira, S.G. Efimova, A.M. Shchetinin et al., Porous structure of polysulfonamide fibres. Fibre Chem. **10**, 545–550 (1979). https://doi.org/10.1007/bf00546091
8. J. Wang, W. Dong, J. Yu et al., Morphology and performance changes of aromatic polysulphonamide fibres formed by dry jet-wet spinning process. Mater. Res. Innov. **19**, S9-273–S279-277 (2015). https://doi.org/10.1179/1432891715Z.0000000001985
9. H. Li, Y. Zhu, B. Xu et al., Preparation and characterization of all para-position polysulfonamide fiber. J. Appl. Polym. Sci. **127**, 342–348 (2012). https://doi.org/10.1002/app.37896
10. N.I. Muraveva, A.A. Konkin, The molecular weight of the polymer and the conditions of stretching as factors in the properties of fibre from aromatic polysulphonamide. Fibre Chem. **4**, 127–129 (1973). https://doi.org/10.1007/bf00543044
11. I. Stuhlmann, Tanlon PSA fibers for flame-and fire-resistant textiles. Melliand China **3**, 64–68 (2008). https://doi.org/10.3969/j.issn.1007-6867.2009.03.017
12. X. Yang, J. Yu, F. Tian et al., The combined effect of heat-draw ratios and residence time on the morphology and property of aromatic copolysulfonamide fibers. RSC Adv. **5**, 27163–27167 (2015). https://doi.org/10.1039/C5RA01868D
13. J. Yu, R. Wang, C. Yang et al., Morphology and structure changes of aromatic copolysulfonamide fibers heat-drawn at various temperatures. Polym. Int. **63**, 2084–2090 (2014). https://doi.org/10.1002/pi.4747
14. D.B. Kim, J.J. Pak, S.M. Jo et al., Dry jet-wet spinning of cellulose/N-Methylmorpholine N-oxide hydrate solutions and physical properties of lyocell fibers. Text. Res. J. **75**, 331–341 (2005). https://doi.org/10.1177/0040517505054852
15. B. Qian, D. Pan, Z. Wu, The mechanism and characteristics of dry-jet wet-spinning of acrylic fibers. Adv. Polym. Technol. **6**, 509–529 (1986). https://doi.org/10.1002/adv.1986.060060408
16. M. Suzuki, T. Tanigami, S. Matsuzawa et al., Influence of molecular weight and syndiotacticity on the structure of high-performance poly(vinyl alcohol) fibers prepared by gel spinning. J. Appl. Polym. Sci. **86**, 1970–1977 (2002). https://doi.org/10.1002/app.11118
17. L.K.J. Hauru, M. Hummel, A. Michud et al., Dry jet-wet spinning of strong cellulose filaments from ionic liquid solution. Cellulose **21**, 4471–4481 (2014). https://doi.org/10.1007/s10570-014-0414-0
18. D. Ahmed, Z. Hongpeng, K. Haijuan et al., Microstructural developments of poly (p-phenylene terephthalamide) fibers during heat treatment process: a review. Mater. Res.-Ibero-Am. J. **17**, 1180–1200 (2014). https://doi.org/10.1590/1516-1439.250313
19. T. Zhang, J. Jin, S. Yang et al., Coagulation condition effects on the structures and properties of dihydroxy poly(p-phenylene Benzobisoxazole) (DHPBO) nascent fibers prepared by dry-Jet wet-spinning process. J. Macromol. Sci. Phys. **49**, 487–494 (2010). https://doi.org/10.1080/00222341003595345
20. L. Xu, Study on the surface of PAN fiber in wet-spinning and dry-jet spinning. Hi-Tech Fiber Appl. **26**, 21–24 (2001). https://doi.org/10.3969/j.issn.1007-9815.2001.02.005
21. J. Yu, F. Tian, S. Chen et al., Structure and property development of aromatic copolysulfonamide fibers during wet spinning process. J. Appl. Polym. Sci. **132**, 42343 (2015). https://doi.org/10.1002/app.42343

22. J. Che, C. Burger, S. Toki et al., Crystal and crystallites structure of natural rubber and synthetic cis-1, 4-polyisoprene by a new two dimensional wide angle X-ray diffraction simulation method. I. Strain-induced crystallization. Macromolecules **46**, 4520–4528 (2013). https://doi.org/10.1021/ma400420k
23. S. Ran, D. Fang, X. Zong et al., Structural changes during deformation of Kevlar fibers via on-line synchrotron SAXS/WAXD techniques. Polymer **42**, 1601–1612 (2001). https://doi.org/10.1016/s0032-3861(00)00460-2
24. W. Hoogsteen, G. Ten Brinke, A.J. Pennings, SAXS experiments on gel-spun polyethylene fibres. J. Mater. Sci. **25**, 1551–1556 (1990). https://doi.org/10.1007/bf01045350
25. S. Toki, B.S. Hsiao, S. Kohjiya et al., Synchrotron X-ray studies of vulcanized rubbers and thermoplastic elastomers. Rubber Chem. Technol. **79**, 460–488 (2006). https://doi.org/10.5254/1.3547946
26. X. Jin, J. Wang, Y. Li et al., In-situ SAXS study on self-assembly of copolymer PS-b-PAA. Nucl. Tech. **41**, 080102 (2018). https://doi.org/10.11889/j.0253-3219.2018.hjs.41.080102. **(in Chinese)**
27. N.S. Murthy, C. Bednarczyk, R.A.F. Moore et al., Analysis of small-angle X-ray scattering from fibers: structural changes in nylon 6 upon drawing and annealing. J. Polym. Sci. Pt. B-Polym. Phys. **34**, 821–835 (1996). https://doi.org/10.1002/(sici)1099-0488(19960415)34:5%3c821:aid-polb1%3e3.0.co;2-p
28. Z. Bian, X. Miao, J. Lin, F. Tian, Extraction and structural investigation of jute cellulose nanofibers. Nucl. Sci. Tech. **29**, 106 (2018). https://doi.org/10.1007/s41365-018-0433-x
29. N.P. Kruchinin, T.A. Spirova, V.A. Medvedev et al., Morphological and structural features of polyacrylonitrile fibres spun by the dry-wet method. Fibre Chem. **23**, 169–174 (1992). https://doi.org/10.1007/bf00545854